Synergy between gold and oxygen vacancies in gold supported on Zr-doped ceria catalysts for the CO oxidation

O.H. Laguna*, A. Pérez, M.A. Centeno, J.A. Odriozola

Instituto de Ciencia de Materiales de Sevilla. Calle Américo Vespucio, 49.
CP: 41092 – Seville - Spain

(*) Corresponding author: ohlaguna@icmse.csic.es

Abstract

The CO oxidation activity of 1 wt.% gold catalysts prepared by deposition-precipitation on a series of ceria doped with Zr supports was studied. The supports (10, 25 and 50 Zr At. %) were synthesized by a pseudo sol-gel method through the thermal decomposition of the corresponding metallic propionates. All the prepared solids were characterized by means of XRF, BET, XRD, Raman spectroscopy, SEM, and H_2-TPR. Solid solution was obtained in all mixed systems, while the segregation of different Ce-Zr oxides was observed for the solid with the 50 Zr At. %. The oxygen vacancies population and the amount of easier reducible Ce^{4+} species in the solids increase with the Zr content. No major textural or structural modifications were detected after gold deposition, although a strong Au-support interaction was generated. Such interaction is strongly influenced by the nucleation of gold deposits on the oxygen vacancies and consequently the amount of Zr inserted in the ceria network also determines the dispersion of gold. The presence of gold eases the surface reduction at lower temperatures, and as higher the amount of Zr in the gold catalysts, higher the CO conversion at low temperatures, probably due to the enhancement of the electronic transfer at the surface of the catalysts.

Keywords

Ce-Zr; CO oxidation, oxygen vacancies, gold nanoparticles

1. Introduction

CeO_2-ZrO_2 mixed oxides has been widely studied because its application as three-way catalyst (TWC) promoters [1]. Apart from this use, materials based on these mixed systems have been reported in H_2 production from hydrocarbons [2], sulfur abatement in the fluid catalytic cracking (FCC) process [3], water gas shift reaction (WGS) [4], and as solid oxide fuel cell anodes [5].

The wide range of applications of CeO_2-ZrO_2 mixed oxides is based on their ability to promote noble metal dispersion, and to enhance oxidation reaction processes by employing lattice oxygen. The last feature is allowed by the rapid reduction/oxidation cycles according to the redox reaction: $Ce^{4+} + e^- \leftrightarrows Ce^{3+}$. This results in the ability to store oxygen under lean conditions and to release oxygen under rich conditions, which is known as oxygen storage capacity (OSC) [6]. The intrinsic OSC of CeO_2 is the key for its application as an ionic conductor. The generation of Ce^{3+} species in the reduction process is accompanied with the formation of oxygen vacancies in order to maintain the charge equilibrium. These may be located at the bulk or at the surface of the material, presenting differences of only one order of magnitude between the oxygen diffusivity in the bulk and over the surface. Oxygen vacancies are punctual defects that may alter the geometric and electronic structure as well as the chemical properties of the oxide. Kosacki et al. [7] have studied lattice defects in nanocrystalline CeO_2 thin films and pointed out that the formation enthalpy of the oxygen vacancies can be diminished by lowering the crystallite size, promoting the formation of Ce^{3+} species, especially at the surface of the material, since these punctual defects tend to migrate there in order to reduce the free Gibbs energy of the system.

Considering the relevance of the oxygen vacancies in the ionic mobility in ceria, several efforts have been devoted to increase the population of these defects and the doping with Zr has demonstrated to allow it [8-11]. The use of Zr as modifier of ceria has been widely reported not only by the improvement of the oxygen mobility but also for the enhancement of the thermal stability. Actually,

the thermal stability and the modification of the textural properties have been closely related to the OSC promotion. Besides this, Di Monte et al. [1] drew attention to a number of relevant questions related to Ce-Zr mixed systems that still remain open such as which is the adequate amount of Zr for obtaining an optimal redox and thermal stability. One of the most relevant remarks not usually considered is that the limited solubility of ZrO_2 in the CeO_2 lattice may produce metastable phases. Thus, several domain-type structures hardly detectable by means of conventional characterization techniques could be obtained during the synthesis. Consequently, the no detection of such inhomogeneities may drive to errors when comparing materials with similar compositions [1]. For that reason, there is not yet a general agreement in the optimal content of Zr for achieving the highest thermal stability or OSC in doped ceria solids.

For instance, Trovarelli et al. [12] established $Ce_{0.8}Zr_{0.2}O_2$ as the most stable composition in $Ce_XZr_{1-X}O_2$ materials. Kaspar et al. [13] suggested that the increase of CeO_2 content in $Ce_XZr_{1-X}O_2$ mixed oxides produces the increase of BET area and solids with a ceria content superior than that of $Ce_{0.4}Zr_{0.6}O_2$ may be are candidates for low to medium temperature catalytic applications, avoiding the phase segregation. On the other hand, Masui et al. [14] presented the synthesis of $Ce_{0.5}Zr_{0.5}O_2$ employing different experimental procedures and the evolution of a cubic pyrochlore-type structure was detected in some cases. This is an interesting result because such materials presents ordered structural oxygen vacancies preferably making them more stable.

From these studies, and taking into account the different discussions about the structural modifications in such oxides, the challenge of finding a way to control the oxygen mobility and the thermal stability is open. Despite this, it is clear that the Ce-Zr mixed oxides are good candidates for the deposition of gold nanoparticles, since their oxygen vacancies may act as gold nucleation centers [15-17].

Since Haruta's pioneering work, it has been widely probed that when depositing gold on different supports as ultra-fine particles its chemistry changes

dramatically, becoming extraordinarily active in oxidation reactions at low temperature [18, 19]. Doped ceria oxides have been used for the preparation of gold catalysts looking for small sizes of the gold nanoparticles, and several authors have demonstrated a direct relationship between the oxygen vacancies population in the support and the achieved metallic dispersion of gold [10, 20-23].

Gold supported on Zr-doped ceria has been reported as active catalysts in different processes, not only oxidation reactions, where the electronic interaction between the support and the gold nanoparticles plays a determinant role. For instance Pojanavaraphan et al. [16] have tested bimetallic Au-Cu/$Ce_{0.75}Zr_{0.25}O_2$ catalysts in the steam reforming of methanol (SRM). The analyzed homogeneous Au-Cu alloys (achieved with 1/3 Au/Cu molar ratio) were active in the SRM but only the catalyst with a 7 wt.% Au-Cu presented a total methanol conversion at 300 ºC. The presence of oxygen vacancies was reported to be relevant not only for the improvement of the dispersion of Au and Cu, but also for the ability to activate oxygen which is crucial for the carbon gasification. The authors hypothesized that in the Au-Cu/$Ce_{0.75}Zr_{0.25}O_2$ catalysts, the coke formation is reduced during reaction, since Cu is able to activate molecular O_2 close to Au sites, where the oxygen molecules react with the coke. This results in an important inhibition of the principal deactivation process of the catalyst during the SRM.

On the other hand, Perret et al. [24] have synthesized Au/$Ce_{0.62}Zr_{0.38}O_2$ for the selective hydrogenation of benzoic acid in order to produce benzyl alcohol. The easy production of oxygen vacancies by the inclusion of Zr drives to the hydrogenation of an aqueous benzoic acid feed towards benzaldehyde and benzyl alcohol with a high rate because of the activation of the carboxyl function for hydrogen attack by the oxygen vacancies.

For a series of Ce-Zr solids tested in the water gas shift reaction, Vindigni et al. [17] observed the following sequence of catalytic activity: AuCe50Zr50 > AuCe80Zr20 > AuCe. The higher catalytic activity showed for the AuCe50Zr50 sample was attributed not only to the higher dispersion of the deposits of gold,

but also to its increased acid/base properties. The strong interaction between gold clusters and oxygen vacancies may generate some partially negative charged gold nanoparticles that may participate as active sites in the reaction.

Considering the scenario presented above, a wide number of papers devoted to the study of Ce-Zr mixed oxides may be found in literature. Nevertheless the existence of an optimal Ce/Zr molar ratio for achievement of the maximum improvement of the oxygen mobility in Zr-doped ceria is a question that remains unresolved. In this sense, this article aims fist to share different points of view presented in literature and to correlate them through a comparison with our own experimental results. Secondly, the influence of the structural modifications of Zr-doped ceria over the promotion of gold nanoparticles and their applying as CO oxidation catalysts is also discussed. For that purpose, the synthesis of Zr-doped ceria supports, varying the Zr atomic percentage (10, 25 and 50) is proposed. These solids are employed for the preparation by deposition-precipitation of 1 wt.% gold catalysts. The obtained materials are characterized by means of X-ray fluorescence (XRF), N_2 adsorption, X-ray diffraction, Raman spectroscopy, scanning electronic microscopy, and H_2-TPR. The generated results allows establishing clear trends of the structural modifications and the reducibility of the materials, that will be correlated with the catalytic activity of the solids, evaluated in the CO oxidation reaction.

2. Materials and methods

2.2. Synthesis of the supports

A series of Ce-Zr mixed oxides, with different Zr atomic percentages (Zr At.% = 10, 25 and 50 calculated according Eq. 1) were synthesized by modifying a reported pseudo sol-gel method involving the thermal decomposition of the propionates of the respective cations. The adequate amounts of Ce (III) acetate (Aldrich®), and Zr (IV) acetyl acetonate (Aldrich®) were dissolved in propionic acid (Alpha Aesar®) (0.12 M). The propionic acid excess was distilled until obtaining a resin-like solid that was calcined at 500 °C (2 °C/min) for 2 h. Pure CeO_2 was synthesized by the same procedure for comparative purposes.

$$ZrAt.\% = \frac{Zr(atoms)}{\left[Ce(atoms) + Zr(atoms)\right]} \times 100 \qquad \text{Eq. 1}$$

Gold catalysts were prepared by deposition–precipitation. The adequate amount of $HAuCl_4 \cdot 3H_2O$ to obtain 1% w/w of gold in the support, was dissolved in deionized water (6.0×10^{-4} M) and the pH of the solution was adjusted to 8 by addition of NaOH 0.1 M with an automatic system of measurement and titration (CRISON® pH-Burette 24). This pH value has been reported as adequate for a successful deposition of gold on ceria surfaces [25]. The solution was heated to 70 °C and then the support was added and kept under continuous stirring for 20 minutes. After that, the solid was filtered and washed with distilled water until the disappearance of Cl^- and Na^+ ions, dried overnight at 100 °C and finally calcined for 2 h at 300 °C.

The nomenclature used for the obtained materials indicates the Zr At.% in every case and the presence of gold for the gold catalysts (CeO_2, CeZr10, CeZr25 and CeZr50 for the supports and Au/CeO_2, Au/CeZr10, Au/CeZr25 and Au/CeZr50).

2.3. Characterization

The elemental composition of the samples was determined by X-ray fluorescence (XRF) spectrometry in a Panalytical AXIOS PW4400 sequential spectrophotometer with Rh tube as source of radiation. The measurements were performed onto pressed pellets containing 6 wt.% wax.

The textural properties were studied by N_2 adsorption/desorption measurements at liquid nitrogen temperature in a Micromeritics ASAP 2010 apparatus. Before analysis, the samples were degassed at 150 ºC for 2 hours under vacuum.

Powder X-ray diffraction (XRD) patterns were recorded on a Siemens D500 diffractometer, using Cu Kα radiation (40 mA, 40 kV), with 0.017° step size and 275 s of step time, over a 2θ range from 10 to 90°.

Raman spectra were recorded in a dispersive Horiva Jobin Yvon LabRam HR800 Confocal Raman Microscope with a green laser (532.14 nm) working at 5 mV power and using a 600 grooves/mm grating. The microscope used a 50x objective with a confocal pinhole of 1000 μm.

Scanning Electron Microscopy (SEM) analyses of the supports were carried out in a SEM-FEG Hitachi® S4800 instrument equipped with an energy dispersive X-ray analyzer (EDX). Concerning the gold catalysts, these were studied with a Zeiss ULTRA 55 high-resolution FESEM equipped with lens, secondary and back-scattered detectors.

Temperature Programmed Reduction (TPR) experiments were carried out in a conventional quartz reactor connected to a TCD. The reactive gas stream (5% H_2 in Ar) was flowed at 50 mL/min over 50 mg of sample and the temperature raised at 10 °C/min from room temperature to 900 °C. A molecular sieve 13X was used to retain the produced H_2O and CO_2. Quantitative analysis was done by integration of the TCD signal and comparison with hydrogen consumption of a CuO reference.

2.4. Catalytic activity

For the oxidation of CO, the solids (80 mg with 100 μm <ø<200 μm particle size) were pretreated for 1 h at 300 ºC in a 30 mL/min activation flow of 21vol% O_2 balanced in He. The light-off curves (from room temperature to 400 ºC, 5ºC/min) were obtained passing a 42 mL/min feed-stream of 3.4 vol.% CO and 21 vol.% O_2 balanced in He. The reaction was carried out in a conventional continuous flow U-shaped quartz reactor working at atmospheric pressure placing the sample between glass wools. The reaction products were followed by mass spectrometry (Balzers® Thermostar) equipped with software Balzers® [26].

This software allows quantification of CO, O_2 and CO_2 by continuously monitoring the selected m/z signals (28, 32 and 44, respectively, previously calibrated) as a function of time and related the observed intensity to that of helium (m/z=4) used as an internal standard.

3. Results and discussion

The chemical composition and the BET surface areas of the prepared supports and the gold catalysts are presented in table 1. In all solids, supports and catalysts, the measured Zr loading is very close to the intended one. In the same way, the gold loading in the catalysts is close to the intended one of 1 wt %.

The N_2 adsorption-desorption experiments (not presented) exhibited IV type isotherms with H2 hysteresis in all cases. These isotherms are typical for mesoporous materials with heterogeneous distribution of the mesopores size. The mixed systems exhibited superior surface areas respect to that of the bare CeO_2, presenting values around 70 m^2/g. This agrees with similar results previously reported for Ce-Zr mixed oxides prepared by coprecipitation [27].

The BET surface area of the Au/CeO_2 is similar to that of the support while those catalysts prepared from the mixed systems exhibited a slight decrease of this value respect to the supports (60 vs.70 m^2/g). The Au/CeZr50 showed a decreasing of its specific BET area after the deposition of gold, even below than that of the CeZr50 support.

The XRD patterns of the synthesized supports and the crystallite sizes calculated with the Scherrer equation are presented in Figure 1. The CeO_2 profile corresponds to the *c*-CeO_2 fluorite structure F*m*3*m* (JCPDS 34394) [28] and the mixed oxides exhibit the same profile. Nevertheless, for these materials, a shift of the diffraction lines to higher 2θ values is observed with the Zr loading. Such behavior can be seen more clearly in Figure 1 inset, where the

shift of the diffraction line associated to the (111) crystallographic plane of CeO_2 is presented.

The modification of the position of the XRD lines of CeO_2 has been widely described for Ce-Zr mixed systems with different Ce/Zr ratios [27, 29-32] and associated to the solid solution formation since the high solubility of Zr cations in the CeO_2 network. A $Ce_1Zr_{1-X}O_2$ solid solution ($0 < X < 1$) is obtained through the isomorphic replacement of Ce^{4+} cations by Zr^{4+} into the structure of ceria. Consequently a contraction of the framework would be expected due to the lower ionic radii of the Zr^{4+} compared to Ce^{4+} (0.84Å and 0,97Å respectively) [33]. In this sense, the distortion of the cell parameters by the isomorphic substitution results in a modification of the cubic symmetry of the CeO_2. Actually the symmetry of the Ce-Zr mixed oxide depends on the Ce/Zr atomic ratio as proposed by Fornasiero et al. [29].

A classification of the crystallographic phase and the space group of Ce-Zr mixed oxides as a function of the Ce At.%, previously proposed by Yashima et al. [34, 35] is presented in Table 2. From this classification, it can be inferred that tetragonal phases are the intermediate structures between the monoclinic and the cubic ones, respectively associated to the bare ZrO_2 and CeO_2 oxides.

The crystallite size values (Figure 1) decrease with the incorporation of Zr until a minimum value obtained for solids with 25 and 50 Zr At.%. Assuming that, smaller the crystallite size greater the exposed area of the crystals, these results agree with the textural ones for the solids doped with 10 and 25 Zr At.%, where higher BET surface areas are observed for the mixed systems compared to that of the CeO_2 (Table 1). Nevertheless the CeZr50 did not present a superior specific area than that of the CeO_2, while no decreasing of its crystalline size below such of the CeZr25 was observed. The decreasing of the crystallite sizes through the doping with Zr evidences that the solid solution formation stabilizes the CeO_2 framework avoiding the sintering during the calcination. The inhibition of the CeO_2 crystallite size growth during the calcination step due to the doping, not only with Zr^{4+} but also with other cations, has been previously evidenced [8, 36, 37]. From these works, it can be inferred

that the structural defects inserted by the doping agents create an energetic barrier that delays the crystallization of the mixed oxide framework.

On the other hand, assuming a cubic structure for all prepared solids, the cell parameter (a) may be calculated using the reflection of the (111) crystallographic plane. If these obtained cell parameters are depicted as a function of the Zr At.% (Figure 2), a linear decreasing correlation is observed as the Zr At.% increases.

This trend agrees with the Vegard's law [38], and points out the high solubility of Zr^{4+} cations in the CeO_2 network [14, 32]. Some authors [39, 40] have observed similar results establishing that, as the Zr content of the solid solution increases, the lattice parameters decrease. This behaviour was confirmed by DFT theoretical studies carried out by Grau-Crespo et al. [41], and related to the smaller ionic radii of the Zr^{4+} cation with respect to Ce^{4+}. These authors also noted that, for a given Ce-Zr composition, it is possible small fluctuations in the cell parameters among different configurations because of slight breakages of the symmetry. Accordingly, the points presented in Figure 2 could represent the average cell parameter of more than one Ce-Zr phases with slight modified compositions. In good agreement with this, a detailed analysis of the XRD patterns of the prepared supports shows an asymmetric broadening of the reflection lines of the CeZr50 solid (Figure 3), which could confirm the existence of more than one crystalline phase.

Taking into account the classification presented in Table 2, and considering the chemical composition of the prepared supports, the CeZr10 solid would present a cubic structure and the CeZr25 and CeZr50 would be in the composition range of tetragonal *t''* and *t'* phases respectively. Nevertheless, the metastable transitions of t phase to *t'* and to *t''* are relatively easily achievable. Consequently, the asymmetry observed for the (220) reflection of CeZr50 (Figure 3), indicates the occurrence of transitions between tetragonal phases (*t'* and/or *t''*), allowing the segregation of more than one mixed oxide ($Ce_XZr_{1-X}O_2$) with variable Ce/Zr atomic ratios. From these results it can be inferred that the Ce/Zr molar ratio in the CeZr50 support is not completely homogeneous

throughout the length of the material, and the respective point in the linear trend presented in Figure 3 present a higher error than those of the other solids.

In their theoretical studies about Ce-Zr mixed oxides, Grau-Crespo and coworkers [41] have calculated the enthalpy of mixing in ceria-zirconia solid solutions obtaining strongly positive values. Consequently, the cation ordering is not a stabilizing factor on these materials. Moreover, the Zr^{4+} cations have an energetic preference to segregate forming a separate Zr-rich phase. Although this process is energetically enhanced, the diffusion of the $Ce^{4+}$and Zr^{4+} cations to the segregated phases is not easy from the kinetic point of view, requiring very high temperatures for occurring (near to 1000 ºC). Therefore, the kinetic barrier for the diffusion of cations may protect the formation of metastable homogeneous Ce-Zr mixed systems for certain chemical compositions in temperature ranges of operations adequate for catalytic applications. In our case, all the supports were calcined at 500 ºC, and monophasic systems are obtained for 10 and 25 Zr At.%. However, for the CeZr50 sample, the high amount of doping agent easies the segregation, and although a tetragonal (t') phase is expected (according to Table 2), the coexistence of more than one tetragonal phase is probable.

The relevance of selecting an adequate synthesis procedure in order to control the homogeneity of the material is evident. Therefore, variables such as the nature of the metallic precursors and the procedure for improving the Ce-Zr interaction are of capital relevance during the preparation of these mixed oxides. In our case, the use of propionates is founded on the hypothesis that the organic anion may act as a pseudo-template that allows ordering of the Ce^{3+} and Zr^{4+} cations during their intimate contact. Then, during the calcination step, this order would be preserved by means of the slow decomposition of the propionates until consolidating the mixed oxide structure. According to that, the temperature and the rate for the calcination are relevant on determining homogeneity of the solid since the achievement of a singular or multiphase system, especially when the chemical composition allows obtaining easy transitions between metastable phases.

The evolution of segregated phases in Ce-Zr mixed oxides with different chemical composition have been evidenced by other authors such as Fornasiero et al. [29], especially for solids with high Zr At.%. For instance, in their studies over a $Ce_{0.5}Zr_{0.5}O_2$ mixed oxide, they observed an asymmetric broadening of the diffraction line associated to the crystallographic plane (220), which is in good agreement with that presented in Figure 3 for our CeZr50 sample. They proposed a deconvolution of the XRD pattern in two profiles. One of them is related to the mixed oxide and the other one to a small portion of unmodified CeO_2. Similarly, S. Bernal et al. [27] reported the separation of two phases ($Ce_{0.8}Zr_{0.2}O_2$ and $Ce_{0.2}Zr_{0.8}O_2$) when a 50 Zr At.% was employed for doping the CeO_2 structure.

The XRD patterns of the gold catalysts are presented in Figure 4. No modifications of the main reflections associated to the correspondent supports were detected, which suggests that no structural distortions have been achieved by the inclusion of the noble metal. On the other hand, no relevant modifications of the crystallite size were detected, compared with the supports (Figure 1).

No XRD signals associated with any gold crystalline phases were detected, which can be due to the low content of such metal or, more probably, to the high dispersion of the gold nanoparticles, as early reported for gold supported on modified ceria catalysts prepared by the same propionates decomposition method [8].

The Raman spectra of the supports and those of the gold catalysts are presented in Figures 5 and 6 respectively. For the bare CeO_2, two main signals can be observed. The more intense one (460 cm^{-1}) corresponds to the F_{2g} Raman active mode of CeO_2 fluorite structure, due to the asymmetric breathing mode of the oxygen atoms around Ce^{4+} cations. The other weak band detected (600 cm^{-1}) has been associated to oxygen vacancies in the framework [8, 42, 43].

The Ce-Zr mixed systems also present the Raman bands characteristic of pure CeO_2. Nevertheless, some remarkable modifications of these signals are detected. For instance, the F_{2g} band becomes broader and shifts to higher energies (positive Raman shift) with the Zr At.%. These alterations indicate the modification of the vibrational structure of the CeO_2. In this sense, Graham et al. [44] have proposed an empirical method for determining the particle size of CeO_2 using the linear increasing of the half-width of the F_{2g} signal with the inverse particle size. They observed that when the particle size decreases, the F_{2g} line becomes broader. Our results agree with this observation, since the XRD data evidence that the inclusion of Zr results in the decrease of the crystallite size (Figure 1). Despite this, the same author has proposed that as the half-width of the F_{2g} signal became broader, the position of such shifted to lower values of Raman shift, which is opposite to our results.

The Raman shift of the F_{2g} signal of the CeO_2 that in our case increases with the Zr At.%, is determined by the particle size as discussed above, but also may be influenced by distortions of the relaxation energy of the phonon promoted by alteration of the oxide structure. For our Ce-Zr materials, such structural alteration is produced by the inclusion of Zr into the cubic ceria lattice [44]. The modification of the vibrational states of the CeO_2 by doping with other elements, resulting in the alteration of the main signals of the Raman Spectra, has been described early. For instance in a study of doped ceria catalysts with flowerlike morphology for the CO oxidation, Xiao et al. [37] presented the Raman spectra of different materials, and the F_{2g} signal shifted as the dopant cation changed (Y, La, Pr, Zr and Sn), resulting in positive or negative shifts respect to the position of the F_{2g} signal of the bare CeO_2. This behavior was directly associated to the alteration of the crystallite size in the same way than for the materials prepared in our work.

Similarly, we have recently compared the doping of CeO_2 with Zr, Zn and Fe. In the three cases, the crystallite size decreased compared with that of the bare CeO_2 oxide, and the F_{2g} Raman band became broader. Also, a positive shift of this Raman band for the Zr- and Zn-modified solids, while a negative one for the Fe-doped solid, was observed. These results demonstrated that depending on

the chemical nature of the doping agent, the alteration of the vibrational states may be carried out in different ways.

Another interesting feature of the Raman spectra of the doped systems is the evolution of a new broad signal around 260 cm^{-1}. This signal is blue shifted (indicated by the pink arrow in Figure 5) with the Zr At.%, which suggests a progressive tetragonalization of the structure. The identification of the type of the produced tetragonal phase is difficult from the Raman results, due to the easy transition between the different *t* symmetries [29, 34, 35] as was discussed above. Particularly in the case of the CeZr50 solid, the possible coexistence of more than one tetragonal phase makes the distinguishing of the possible structures hardly achievable.

The tetragonalization of the cubic structure by the inclusion of Zr is also related to the evolution of the oxygen vacancies signal, which increases with the Zr At.%. Ganduglia-Pirovano et al. [45] have proposed that the main effect of the up-taking of oxygen species is the important change in the nature of the f electrons namely from valence to core-like. Consequently, the presence of oxygen vacancies represents an alteration of the symmetry and the electronic distribution of the network which is evenly shared by all the metallic atoms of the oxide. Therefore, the evolution of the oxygen vacancies signal observed in the Raman spectra is a consequence of the modification of the electronic distribution of the oxides that would be correlated with the amount of doping agent, which is responsible of the alteration of the textural and structural properties of the materials.

As presented in recent works, a correct evaluation of the evolution of oxygen vacancies population in pure and doped cerium oxides must be carried out by comparing the area ratio of the oxygen vacancies band and the F_{2g} signal (Ov/F_{2g}) [8, 42, 43] in order to reduce the possible influence of the particle size and other effects over the shape and intensity of the signals [8, 43, 46, 47]. The Figure 5 inset shows how the population of oxygen vacancies increases with the Zr At.% in our materials.

The oxygen vacancies formation may be thermodynamically enhanced by the reduction of the crystallite size, according to Kosacki et al. [7]. They have studied lattice defects in nanocrystalline CeO_2 thin films and pointed out that the formation enthalpy of the oxygen vacancies can be reduced by a lower crystallite sizes, promoting the presence of more Ce^{3+} species, especially in the surface of the material, because these punctual defects tend to migrate to the surface in order to reduce the free Gibbs energy of the system. That described above is in good agreement with our observation of the increment of the oxygen vacancies population and the reduction of the crystallite size of the studied Ce-Zr mixed systems.

The Raman spectra of the gold catalysts are presented in Figure 6. The F_{2g} signal stills being the more intense in all cases, but it is redshifted compared with the supports presented in Figure 5 (440 cm^{-1} and 460 cm^{-1} respectively). If the position of such Raman signal is strongly influenced by the electronic environment of the CeO_2 structure, the observed blue shift may be attributed to the electronic interaction between gold clusters and the structure of the support, moreover if the ceria crystallite size is not affected by the gold presence, as in our case.

Despite the observed interaction between gold and the supports, there were not significant differences in the position of the F_{2g} signal for the gold catalysts. However, the most relevant feature of the Raman spectra is the absence of the oxygen vacancies signal and the strong reduction of the intensity of the signals below 300 cm^{-1} associated to the tetragonalization of the oxide. This behavior must be related to the interaction between the surface and the gold species. Some authors have established that oxygen vacancies can act as preferential structural sites for the selective deposition of gold, which would increase the dispersion of the noble metal [45, 48-51]. The interaction of the oxygen vacancies in CeO_2 with other metals such as Rh, Ir, Pd and Pt has been also observed and associated to a metal-support strong interaction model, named metal nesting, by the filling of the oxygen vacancies with the metallic atoms [52].

The observed interaction of gold and the oxygen vacancies allows considering the possibility that higher the population of oxygen vacancies in the support, higher the gold dispersion in the catalysts. However, the vanishing of the Ov signal after the deposition of gold suggests that the most oxygen vacancies detected were located preferentially at the surface of the supports, and in our case, a bulk to surface oxygen vacancies low ratio may occurring. This is in good agreement with the fact that formation of oxygen vacancies within the bulk is also feasible but less thermodynamically favored that the formation of surface oxygen vacancies. Moreover, despite the possible creation of oxygen vacancies in the bulk, these punctual defects tend to migrate to the surface in order to minimize the Gibbs free energy [53], therefore a homogeneous distribution of these defects along the extension of the material is hardly achievable. In this sense, a superior energetic barrier for the creation of oxygen vacancies at the bulk in CeO_2 than in the surface of such material has been recently proposed by Plata et al. [54] employing DFT calculations for a model of a multilayer structure of CeO_2 linked to a Yttrium-stabilized zirconia (YSZ), being 2.42 eV for the vacancies at the bulk and 1.72 eV at the surface of the CeO_2 phase.

The surface character of most of oxygen vacancies which were detected for the Ce-Zr mixed oxides through the Raman spectra has been previously suggested for a similar system (Eu-doped ceria [43]) evaluated under the same experimental conditions that our material. In this work it was considered that using a laser line where the optical absorption exists, the majority of excitation laser and scattering light were adsorbed by the sample. Then, only a portion of the radiation escaped, and the Raman signal got weak, containing information preferentially of the surface of the solids.

Representative SEM micrographs of the supports and the average chemical composition determined by EDX from 10 measurements at different zones of the sample are presented in Figure 7.

Pure CeO_2 exhibited a laminated morphology with layers being composed by wormlike aggregates. Some gaps, that give rise to mesopores and macropores, remain at the junction of the aggregates (Figure 7a). On the other hand, the Ce-

Zr mixed systems present a randomly junction of the aggregates, without the layered structure of the bare CeO_2.

Zr At.% values calculated by EDX analysis agree with XRF ones (see Table 1). It means that there is an acceptable homogeneity of the Zr species along the materials. Despite the good correlation, a slight discrepancy is detected in the case of the CeZr50 solid. This is probably related to the segregation of different Ce-Zr mixed phases, with variable Ce/Zr molar ratios.

In order to analyze the dispersion of the gold nanoparticles over the catalysts, a high resolution field emission scanning microscopy (FESEM) study was carried out. Selected micrographs are presented in Figure 8.

The main change in morphology is observed in Au/CeO_2, where the layered structure of the support is not detected. In addition, this material exhibits bright spots with diameters between 20 and 30 nm, probably associated to Au particles. These bright spots are not observed for the catalysts containing Zr. Since all catalysts present the same loading of gold, the absence of a high density of appreciable bright spots in the materials with Zr (Figures 8b and 8c) must be related with a higher metallic dispersion. However, the low contrast between Au and Ce due to their similar molar weight makes hardly observable by SEM the differences in metallic dispersion between the gold catalysts. This observation agrees with the higher interaction between the gold nanoparticles and the surface of the supports, especially with the oxygen vacancies, evidenced and discussed in the Raman results. Therefore, a higher oxygen vacancies concentration at the surface of the support results in a higher dispersion of the gold nanoparticles. Similar results have been recently presented for similar gold catalysts prepared over doped-ceria supports [8, 55], confirming the role of preferential sites for the nucleation of gold nanoparticles of the oxygen vacancies.

The H_2-TPR profiles of the bare CeO_2 and the mixed oxides are presented in Figure 9. Pure CeO_2 presents two main signals that have been widely described for such oxide. The initial occurrence of the low temperature signal (centered at

470 °C in our case) is due to the surface reduction of Ce^{4+} cations into Ce^{3+}, while the high temperature signal (with maximum at 754 °C) is associated to Ce^{4+} to Ce^{3+} reduction in the bulk [8, 29, 30, 56, 57].

The high temperature signal also presents a shoulder at 884 °C that may be associated to the reduction of some Ce^{4+} cations in a deeper position into the bulk less exposed. The presence of different reduction events for the CeO_2 at high temperature has been previously described and related with different reductions kinetics in the bulk [29, 58].

Ce-Zr mixed oxides also present two main reduction events at low and high temperatures, only due to the reduction of Ce^{4+} cations because the Zr^{4+} ones are not reducible [28]. Nevertheless, the intensity of the low temperature event is considerably higher than that of the high temperature reduction one for all the mixed oxides, which is in opposite way to that observed for the bare CeO_2. On the other hand, the maximum intensity of the low temperature reduction process shows a slight shift to higher temperatures with increasing the Zr At.%. This suggests that the doping with Zr increases the population of more easily reducible Ce^{4+} cations but the required energy for the reduction of the additional Ce^{4+} cations progressively increases. Since the reduction of Ce^{4+} results in the creation of new oxygen vacancies, the observed shift of the low temperature peak may be indicative of the enhancement of the energetic barrier for the creation additional oxygen vacancies, as was proved by Krcha et al. [59] in their theoretical study applying DFT+U methods on transition metal-doped CeO_2. They demonstrated the decreasing of the energy vacancy formation (ΔE_{vac}) in CeO_2 in the nearest neighbor, by doping it with Zr (from 2.76 to 1.63 eV). On the other hand, even after the doping with Zr, the ΔE_{vac} for the creation of new oxygen vacancies in the next nearest neighbor was superior (2.61 eV), which may be the reason for the progressive shift to higher temperatures of the low temperature reduction peak in the TPR profiles of our supports (Figure 9).

The improvement of oxygen storage capacity, redox properties and oxygen mobility in ceria by the Ce^{4+}/Zr^{4+} isomorphous substitution, which is in good agreement with the TPR results presented in Figure 9, has been also reported [14, 60]. Such enhancement of the redox properties in the mixed oxides also correlates with the strong interaction between Ce^{4+} and Zr^{4+} cations deduced by the XRD patterns and with the alteration of the symmetry observed through the Raman spectroscopy.

An inadequate discussion of some nuances in explaining the results of reducibility may result in controversial discussions about the enhancement or detriment of the reducibility in Ce-Zr mixed oxides depending on the loading of Zr, as was pointed out by Vidal et al. [56]. Nevertheless, most authors claim a beneficial effect in the ceria reducibility by the addition of Zr because of the increasing of the population of surface Ce^{4+} reducible cations, even if the maximum temperature of the low temperature reduction becomes higher than for the pure CeO_2.

The TPR profiles of gold catalysts are presented in Figure 10. For the Au/CeO_2 solid, two main peaks at low and high temperature are observed as for pure CeO_2. However, the low temperature one occurs at a lower temperature and is more intense than the high temperature peak. Considering that gold must be present on the surface of the support in close interaction with the oxygen vacancies, as was demonstrated by Raman, such interaction could be also responsible of the improvement of the redox properties, not only by increasing the population of reducible Ce^{4+} cations at the surface of the CeO_2, but also for carrying out this process at less temperature as will be discussed below.

The gold catalysts synthesized with the mixed oxides also present both low and high temperature reduction events. The low temperature signals become broader as the amount of Zr increases, even becoming noticeable the contribution of more than one reduction process. At high temperatures, a broad zone of reduction is observed between 400 and 900 ºC. The area of this high peak clearly decreases by increasing the amount of Zr in the solid, which must

be related with the improvement of the reducibility due to the Au-Ce-Zr not only at the surface but also in the bulk.

This enhancement of the reducibility of CeO_2 and Ce-Zr mixed oxides by the deposition of gold has been reported previously by Fonseca et al. [61]. In their work, the ability of Au and Pt to promote the reducibility of CeO_2 and $CeZrO_4$ is compared. Although both noble metals showed similar shifts in the reduction profile of CeO_2, they suggested that gold was less effective in the modification of the reduction degree of CeO_2, because it only enhanced the reduction of surface and near-surface Ce^{4+}, while Pt allows an easy reduction of both surface and bulk Ce^{4+}. Our results partially agree with this observation because, although the main contribution on the reducibility after the deposition of gold seems to be over the surface Ce^{4+}, the reduction bulk cations seems to be progressively affected also with the increasing amount of Zr.

The generation of oxygen vacancies by the inclusion of Zr in the CeO_2 framework and the strong interaction of such defects with gold nanoparticles influence features such as the final gold particle size in this type of catalysts, through the enhancement of the electronic transfer between the support and the noble metal clusters allowing a higher dispersion, as proposed from SEM (Figure 8).

The electronic transfer between gold and CeO_2 surfaces has been previously proposed by DFT calculations [23]. Au may weaken the bond of the surrounding oxygen atoms, making ceria a better oxidant, which in our case may be understood as better reducible material. In terms of the improvement of the reducibility of ceria through the creation of oxygen vacancies, the electronic transferring, promoted between the surface and the gold deposits, may reduce the energy barrier for creating more of such punctual defects at the surface [15].

On the other hand, the presence of several reduction events not only for gold catalysts but also for the supports (Figures 9 and 10) resulted in broad TPR profiles where the deconvolution is hardly achievable, and differentiation between surface or bulk reductions is difficult. Nevertheless, the total amount of

H_2 consumption during each complete experiment, normalized by the loading of sample or the amount of reducible material, allows establishing a semi-quantification of the reducible species population, which is an additional criterion for comparing the reducibility of the prepared materials.

For that analysis, the reducibility percentage (RP) was calculated according to Eq. 2, defined as the ratio between the experimental H_2 consumption (EHC) measured during the TPR analysis and the theoretical H_2 consumption (THC) if all the Ce^{4+} cations become reduced (Figure 11).

$$RP = \frac{EHC \times 100}{THC} \qquad \text{Eq. 2}$$

In the case of gold catalysts, the possible contribution of cationic gold species was not considered since the Ce/Au atomic ratio in any case is close to 100 times.

For the supports, the RP increases with the loading of Zr. This agrees with the fact that the structure of the mixed oxide is able to stabilize more Ce^{3+} cations than pure ceria. Considering that the ionic radii of Ce^{3+} is higher than those of Ce^{4+} and Zr^{4+}, the possible expansion produced by the Ce^{3+} cations is competing with the contraction produced by the inclusion of Zr^{4+} in the framework of CeO_2 [54]. No matter which of the two effects was more important, the electronic distortion is a phenomenon that greatly favors the ionic mobility. This explains the ability of the doped materials to generate and stabilizing more Ce^{3+} cations.

Concerning the gold catalysts, the RP values present the same trend than for the supports. Although a slight superior amount of reducible species was observed, no considerable differences are evident between each support and its respective gold catalyst. According to these results, the principal contribution of gold to the reducibility of the materials is to facilitate the reduction of reducible species existing at lower temperatures. The more easily reducible species must be those located at the surface of the support, considering that

this is the place where the interaction between the noble metal clusters and the support is happening. The enhancement of the reducibility is another probe of the interaction between gold and the surface, especially with their oxygen vacancies as was proposed from Raman results.

Catalytic activity: CO oxidation reaction

The evaluation of the prepared supports and gold catalysts in the oxidation of CO is presented in Figure 12.

The supports did not present any CO conversion until temperatures above 225 ºC and the highest performance was observed for the CeZr10 and CeZr25 materials, being their catalytic activity very similar between them. Gold catalysts presented a significant improvement of the CO conversion and total CO conversion was achieved at least at 150 ºC in all cases. Concerning the effect of the doping agent, all the mixed systems exhibited a superior catalytic activity than the Au/CeO_2 one at low temperatures. In addition, as the amount of Zr increases, a higher catalytic activity is observed at room temperature (25 ºC).

It is clear that in gold catalysts two effects cooperate for the observed improvement of the CO oxidation ability; i) the creation and stabilization of additional oxygen vacancies, and ii) the promotion of the electronic transfer between the gold nanoparticles and the support. The cooperation of these effects could be understood in terms of the dispersion of gold, because, higher the population of oxygen vacancies, higher the dispersion of the noble metal and higher the possibility for such electronic transfer. However, Chen and Goodman [62] have observed that the CO oxidation ability increases until a maximum value by decreasing the particle sizes of the deposits, near to 3 nm for Au-based catalysts for the CO oxidation reaction. Consequently, the enhancement of the oxygen vacancies population with the amount of Zr and the decreasing of the gold nanoparticles sizes for achieving a higher CO conversion at low temperature must be carefully associated, because depending on the size of the metallic clusters, the CO conversion would be drastically altered.

In good agreement with our results, the enhancement of the catalytic activity in CO oxidation reactions by doping the structure of CeO_2 has been widely evidenced by many authors applying several doping agents: Zn [63], Sm [22], Fe [64], Co, Mn [65], Cu [66, 67] and Eu [43], among others. In these works, the creation of oxygen vacancies by the strong interaction of the CeO_2 framework and the doping cation is commonly proposed as a determinant structural effect that facilitates the adsorption and activation of the CO and O_2 molecules during the catalytic reaction.

Besides this positive effect during the CO oxidation reaction, oxygen vacancies became determinant when gold is deposited on the surface because the strong interaction between them, decreases the required energy for the reduction of the catalyst. The easy reducibility promoted in the gold catalysts can be exploited as high capacity to capture and oxidize CO.

On the other hand, the capital relevance of the gold-oxygen vacancy interaction can be observed in other systems also applied for the CO oxidation reaction. For instance, we have recently reported the enhancement of the electronic transfer in gold catalysts prepared on Y-doped TiO_2 in the CO oxidation reaction [68]. When gold nanoparticles were placed over oxygen vacancies of the support, a large electronic transfer took place from gold to the gaseous oxygen molecule, activating it for the CO oxidation.

The activation of the O_2 molecule was produced because the electronic density was transferred to antibonding orbitals, weakening and lengthening the O-O bond. These results are in agreement with a previous study presented by Chen and Goodman [62] which proposed that electron-rich Au particles, whose present a strong interaction with the support, are crucial for activating molecular O_2 during the CO oxidation. In a similar way, Boronat and Corma [69] studied the role of Au- and Fe-doped anatase TiO_2 in the oxygen activation during the CO oxidation. By means of DFT methods, the authors observed that during the activation of molecular O_2 on isolated and supported gold nanoparticles, the activation energy involved in the O_2 dissociation was directly related with the degree of electron density transfer from the catalyst to the π^* molecular orbitals

of adsorbed O_2, and with the vibration frequency that reflects the strength of the O-O bond [70]. Particularly, the authors remarked the results obtained with the Fe-doped solids because the adsorption of O_2 involved the electronic transfer from the oxide to the molecule, which was activated as a superoxide O_2^- specie, while Fe^{2+} was reoxidized to Fe^{3+}. Therefore combining the ability for the O_2 adsorption and for reducing the activation energy for the creation of oxygen vacancies in the TiO_2 lattice, an enhanced oxidation activity would be expected for the Fe-doped TiO_2. Finally the authors also suggested that strategy of promoting the oxidation activity by doping with gold the titanium oxide has been employed for the same purpose with ceria.

Despite that discussed above, there is not an exclusive mechanism for explaining the CO oxidation reaction. For instance some researchers suggested that the CO oxidation proceeds by a Mars-van Krevelen mechanism [71], and it is widely accepted that factors such as gold particle size, synthesis methods, pretreatment conditions and the nature of support influence the catalytic activity but the CO oxidation are still subject of debate. In particular the role of the support and oxygen supply is controversial as was remarked by Corma et al. [72].

4. Conclusions

The modification of CeO_2 with different Zr At.% (10, 25 and 50) was successfully achieved and the oxygen vacancies population and the reducibility increase with the loading Zr. In all cases a solid solution formation was detected. However, in the case of the 50 Zr At.% system the segregation of different oxides, probably metastable tetragonal symmetries with different Ce/Zr atomic ratios, was also detected. Comparing our results with those presented in literature, it can be pointed out that the evolution of the possible structures not only depends on the chemical composition of the oxide but also in the synthesis procedure applied for obtaining the materials (being relevant the precursors of Zr^{4+} and Ce^{3+} cations, and the calcination program).

No major structural or textural modifications were detected in the solids after the gold deposition, although an electronic interaction between gold nanoparticles and the oxygen vacancies of the supports was observed. Such interaction became stronger as the loading of Zr increased in the solid, leading to an enhancement of the gold dispersion. Gold catalysts did not present a considerable higher population of reducible Ce^{4+} species than the corresponding supports. However, the electronic interaction established between gold and the support surface resulted in the decreasing of the energetic barrier for achieving the reduction of the surface of the solids, which is pointing out the synergy between the oxygen vacancies and the clusters of such noble metal.

Finally, the catalytic activity evaluation in the CO oxidation exhibited wide superior catalytic performance of the gold catalysts compared to the supports. Gold catalysts presented higher CO conversion at temperatures below 150 ºC as the amount of Zr increases. This behaviour may be due to a modified dispersion of gold nanoparticles as the amount of oxygen vacancies population was improved, which is directly related to the Zr loading in the support. The modified dispersion of such noble metal clusters allows the enhancement of the electronic transfer between the catalyst and the reaction environment, and an easier activation of the O_2 molecules.

5. Acknowledgments

The authors thank the financial support from the Ministerio de Economía y Competitividad Español (ENE2012-374301-C03-01 and ENE2013-47880-C3-2-R) co-financed by FEDER funds from the European Union and from Junta de Andalucía (TEP-8196). In addition the authors thank to Dr. Juan Almagro (ACERINOX S.A. Spain) for his help with high-resolution FESEM experiments.

6. References

[1] R. Di Monte, J. Kašpar, Catalysis Today, 100 (2005) 27-35.
[2] H.-S. Roh, K.-W. Jun, S.-E. Park, Applied Catalysis A: General, 251 (2003) 275-283.
[3] B. Wen, M.Y. He, C. Costello, Energy Fuels, 16 (2002) 1048-1053.

[4] L.G. Pinaeva, E.M. Sadovskaya, Y.A. Ivanova, T.G. Kuznetsova, I.P. Prosvirin, V.A. Sadykov, Y. Schuurman, A. C. van Veen, C. Mirodatos, Chemical Engineering Journal, 257 (2014) 281-291.
[5] M. Boaro, A. Pappacena, C. Abate, M. Ferluga, J. Llorca, A. Trovarelli, Journal of Power Sources, 270 (2014) 79-91.
[6] D. Duprez, C. Descorme, T. Birchem, E. Rohart, Topics in Catalysis, 16 (2001) 49-56.
[7] I. Kosacki, T. Suzuki, H.U. Anderson, P. Colomban, Solid State Ionics, 149 (2002) 99-105.
[8] O.H. Laguna, F. Romero Sarria, M.A. Centeno, J.A. Odriozola, Journal of Catalysis, 276 (2010) 360-370.
[9] Q. Jiang, G. Zhou, Z. Jiang, C. Li, Solar Energy, 99 (2014) 55-66.
[10] T.R. Reina, S. Ivanova, M.I. Domínguez, M.A. Centeno, J.A. Odriozola, Applied Catalysis A: General, 419–420 (2012) 58-66.
[11] E.d.O. Jardim, S. Rico-Francés, F. Coloma, E.V. Ramos-Fernández, J. Silvestre-Albero, A. Sepúlveda-Escribano, Applied Catalysis A: General, 487 (2014) 119-129.
[12] A. Trovarelli, C. deLeitenburg, G. Dolcetti, Chemtech, 27 (1997) 32-37.
[13] J. Kaspar, P. Fornasiero, G. Balducci, R. Di Monte, N. Hickey, V. Sergo, Inorganica Chimica Acta, 349 (2003) 217-226.
[14] T. Masui, Y.M. Peng, K. Machida, G. Adachi, Chem. Mat., 10 (1998) 4005-4009.
[15] O.H. Laguna, M.I. Dominguez, F. Romero-Sarria, J.A. Odriozola, M.A. Centeno, CHAPTER 13 Role of Oxygen Vacancies in Gold Oxidation Catalysis, Heterogeneous Gold Catalysts and Catalysis, 2014, The Royal Society of Chemistry, pp. 489-511.
[16] C. Pojanavaraphan, A. Luengnaruemitchai, E. Gulari, Applied Catalysis a-General, 456 (2013) 135-143.
[17] F. Vindigni, M. Manzoli, T. Tabakova, V. Idakiev, F. Boccuzzi, A. Chiorino, Appl. Catal. B-Environ., 125 (2012) 507-515.
[18] M. Haruta, N. Yamada, T. Kobayashi, S. Iijima, Journal of Catalysis, 115 (1989) 301-309.
[19] M. Haruta, Catalysis Today, 36 (1997) 153-166.
[20] T.R. Reina, E. Papadopoulou, S. Palma, S. Ivanova, M.A. Centeno, T. Ioannides, J.A. Odriozola, Applied Catalysis B: Environmental, 150–151 (2014) 554-563.
[21] T.R. Reina, W. Xu, S. Ivanova, M.Á. Centeno, J. Hanson, J.A. Rodriguez, J.A. Odriozola, Catal. Today, 205 (2013) 41-48.
[22] M. Manzoli, G. Avgouropoulos, T. Tabakova, J. Papavasiliou, T. Ioannides, F. Boccuzzi, Catalysis Today, 138 (2008) 239-243.
[23] M. Nolan, V.S. Verdugo, H. Metiu, Surface Science, 602 (2008) 2734-2742.
[24] N. Perret, X.D. Wang, J.J. Delgado, G. Blanco, X.W. Chen, C.M. Olmos, S. Bernal, M.A. Keane, Journal of Catalysis, 317 (2014) 114-125.
[25] M.A. Centeno, C. Portales, I. Carrizosa, J.A. Odriozola, Catal Lett, 102 (2005) 289-297.
[26] O.H. Laguna, M.A. Centeno, F. Romero-Sarria, J.A. Odriozola, Catalysis Today, 172 (2011) 118-123.
[27] G. Colon, M. Pijolat, F. Valdivieso, H. Vidal, J. Kaspar, E. Finocchio, M. Daturi, C. Binet, J.C. Lavalley, R.T. Baker, S. Bernal, J. Chem. Soc.-Faraday Trans., 94 (1998) 3717-3726.
[28] P. Singh, M.S. Hegde, Journal of Solid State Chemistry, 181 (2008) 3248-3256.
[29] P. Fornasiero, G. Balducci, R. Di Monte, J. Kašpar, V. Sergo, G. Gubitosa, A. Ferrero, M. Graziani, Journal of Catalysis, 164 (1996) 173-183.
[30] G. Balducci, P. Fornasiero, R. Dimonte, J. Kaspar, S. Meriani, M. Graziani, Catal Lett, 33 (1995) 193-200.
[31] G. Colón, F. Valdivieso, M. Pijolat, R.T. Baker, J.J. Calvino, S. Bernal, Catalysis Today, 50 (1999) 271-284.
[32] B.M. Reddy, G.K. Reddy, A. Khan, I. Ganesh, J. Mater. Sci., 42 (2007) 3557-3563.
[33] R.D. Shannon, Acta Crystallogr. Sect. A, 32 (1976) 751-767.

[34] M. Yashima, K. Morimoto, N. Ishizawa, M. Yoshimura, Journal of the American Ceramic Society, 76 (1993) 2865-2868.
[35] M. Yashima, H. Arashi, M. Kakihana, M. Yoshimura, Journal of the American Ceramic Society, 77 (1994) 1067-1071.
[36] F. Romero-Sarria, J.C. Vargas, A.C. Roger, A. Kiennemann, Catalysis Today, 133 (2008) 149-153.
[37] G. Xiao, S. Li, H. Li, L. Chen, Microporous and Mesoporous Materials, 120 (2009) 426-431.
[38] A.R. West, Solid State Chemistry and Its Applications, John Willey & Sons Ltd., New York, 1985.
[39] A. Cabanas, J.A. Darr, E. Lester, M. Poliakoff, J. Mater. Chem., 11 (2001) 561-568.
[40] T.A. Lee, C.R. Stanek, K.J. McClellan, J.N. Mitchell, A. Navrotsky, J. Mater. Res., 23 (2008) 1105-1112.
[41] R. Grau-Crespo, N.H. de Leeuw, S. Hamad, U.V. Waghmare, Proceedings of the Royal Society A: Mathematical, Physical and Engineering Science, 467 (2011) 1925-1938.
[42] J.E. Spanier, R.D. Robinson, F. Zheng, S.W. Chan, I.P. Herman, Phys. Rev. B, 64 (2001) 245407 (245401-245408).
[43] W.Y. Hernandez, M.A. Centeno, F. Romero-Sarria, J.A. Odriozola, Journal of Physical Chemistry C, 113 (2009) 5629-5635.
[44] G.W. Graham, W.H. Weber, C.R. Peters, R. Usmen, Journal of Catalysis, 130 (1991) 310-313.
[45] M.V. Ganduglia-Pirovano, A. Hofmann, J. Sauer, Surf. Sci. Rep., 62 (2007) 219-270.
[46] H.Z. Bao, X. Chen, J. Fang, Z.Q. Jiang, W.X. Huang, Catal Lett, 125 (2008) 160-167.
[47] Z.Y. Pu, J.Q. Lu, M.F. Luo, Y.L. Me, Journal of Physical Chemistry C, 111 (2007) 18695-18702.
[48] T. Tabakova, F. Boccuzzi, M. Manzoli, D. Andreeva, Applied Catalysis A: General, 252 (2003) 385-397.
[49] E. Wahlstrom, N. Lopez, R. Schaub, P. Thostrup, A. Ronnau, C. Africh, E. Laegsgaard, J.K. Norskov, F. Besenbacher, Phys. Rev. Lett., 90 (2003) 4.
[50] Y. Wang, G.S. Hwang, Surface Science, 542 (2003) 72-80.
[51] M. Nolan, The Journal of Chemical Physics, 130 (2009) 144702-144709.
[52] M.G. Sanchez, J.L. Gazquez, Journal of Catalysis, 104 (1987) 120-135.
[53] P.J. Gellings, H.J.M. Bouwmeester, Catalysis Today, 12 (1992) 1-101.
[54] J.J. Plata, A.M. Marquez, J.F. Sanz, Chem. Mat., 26 (2014) 3385-3390.
[55] W.Y. Hernandez, F. Romero-Sarria, M.A. Centeno, J.A. Odriozola, Journal of Physical Chemistry C, 114 (2010) 10857-10865.
[56] H. Vidal, J. Kašpar, M. Pijolat, G. Colon, S. Bernal, A. Cordón, V. Perrichon, F. Fally, Applied Catalysis B: Environmental, 27 (2000) 49-63.
[57] H. Vidal, J. Kašpar, M. Pijolat, G. Colon, S. Bernal, A. Cordón, V. Perrichon, F. Fally, Applied Catalysis B: Environmental, 30 (2001) 75-85.
[58] G.R. Rao, J. Kaspar, S. Meriani, R. Dimonte, M. Graziani, Catal Lett, 24 (1994) 107-112.
[59] M.D. Krcha, A.D. Mayernick, M.J. Janik, Journal of Catalysis, 293 (2012) 103-115.
[60] Y. Madier, C. Descorme, A.M. Le Govic, D. Duprez, J. Phys. Chem. B, 103 (1999) 10999-11006.
[61] A.A. Fonseca, J.M. Fisher, D. Ozkaya, M.D. Shannon, D. Thompsett, Topics in Catalysis, 44 (2007) 223-235.
[62] M.S. Chen, D.W. Goodman, Catalysis Today, 111 (2006) 22-33.
[63] A. Penkova, O.H. Laguna, M.A. Centeno, J.A. Odriozola, Journal of Physical Chemistry C, 116 (2012) 5747-5756.

[64] O.H. Laguna, M.A. Centeno, M. Boutonnet, J.A. Odriozola, Applied Catalysis B: Environmental, 106 (2011) 621-629.
[65] L. Ilieva, G. Pantaleo, I. Ivanov, A. Maximova, R. Zanella, Z. Kaszkur, A.M. Venezia, D. Andreeva, Catalysis Today, 158 (2010) 44-55.
[66] O.H. Laguna, M.I. Domínguez, S. Oraá, A. Navajas, G. Arzamendi, L.M. Gandía, M.A. Centeno, M. Montes, J.A. Odriozola, Catalysis Today, 203 (2013) 182-187.
[67] A. Martínez-Arias, A.B. Hungría, G. Munuera, D. Gamarra, Applied Catalysis B: Environmental, 65 (2006) 207-216.
[68] F. Romero-Sarria, J.J. Plata, O.H. Laguna, A.M. Márquez, M.A. Centeno, J.F. Sanz, J.A. Odriozola, RSC Advances, 4 (2014) 13145-13152.
[69] M. Boronat, A. Corma, Catalysis Today, 169 (2011) 52-59.
[70] M. Boronat, A. Corma, Dalton Trans., 39 (2010) 8538-8546.
[71] P. Ghosh, M.F. Camellone, S. Fabris, J. Phys. Chem. Lett., 4 (2013) 2256-2263.
[72] J. Guzman, S. Carrettin, A. Corma, Journal of the American Chemical Society, 127 (2005) 3286-3287.

TABLES

Table 1. Chemical composition and textural properties of the prepared solids

Solids	Zr At.%	Ce At.%	Au wt.%	Specific Area BET (m^2/g)
CeO_2	--	100	--	53
CeZr10	10.3	89.7	--	70
CeZr25	24.9	75.1	--	70
CeZr50	50.2	49.8	--	66
Au/CeO_2	--	100	1.02	54
Au/CeZr10	10.3	89.7	0.97	65
Au/CeZr25	24.5	75.5	1.01	60
Au/CeZr50	50.8	49.2	0.92	53

Table 2. Classification of the phases in Ce-Zr mixed oxides depending on the Ce At.% (Yashima et al. [29,30])

Phase	Ce At.%	Space group
Monoclinic (*m*)	0-20	$P2_1/c$
Tetragonal (*t*)	20-40	$P4_2/nmc$
Tetragonal (*t'*)	40-65	$P4_2/nmc$
Tetragonal (*t''*)	65-80	$P4_2/nmc$
Cubic (*c*)	80-100	F*m*3*m*

FIGURE CAPTIONS

Figure 1. XRD patterns of the Ce-Zr mixed oxides (C.Z = crystallite size calculated by the Scherrer equation)

Figure 2. Cell parameter of the mixed oxides vs Zr At.%

Figure 3. Diffraction lines associated to the crystallographic planes (200) and (220) for the CeO_2 and the CeZr50

Figure 4. XRD patterns of the gold catalysts

Figure 5. Raman spectra of the Ce-Zr mixed oxides

Figure 6. Raman spectra of the gold catalysts

Figure 7. SEM micrographs of the supports: a) CeO_2; b) CeZr10; c) CeZr25; d) CeZr50

Figure 8. SEM micrographs of the gold catalysts: a) Au/CeO_2; b) Au/CeZr10; c) Au/CeZr25

Figure 9. H_2-TPR profiles of the prepared supports

Figure 10. TPR studies of the gold catalysts

Figure 11. Reducibility percentage of the Ce-Zr mixed oxides

Figure 12. Catalytic activity of the Ce-Zr mixed oxides and the gold catalysts

Figure 1

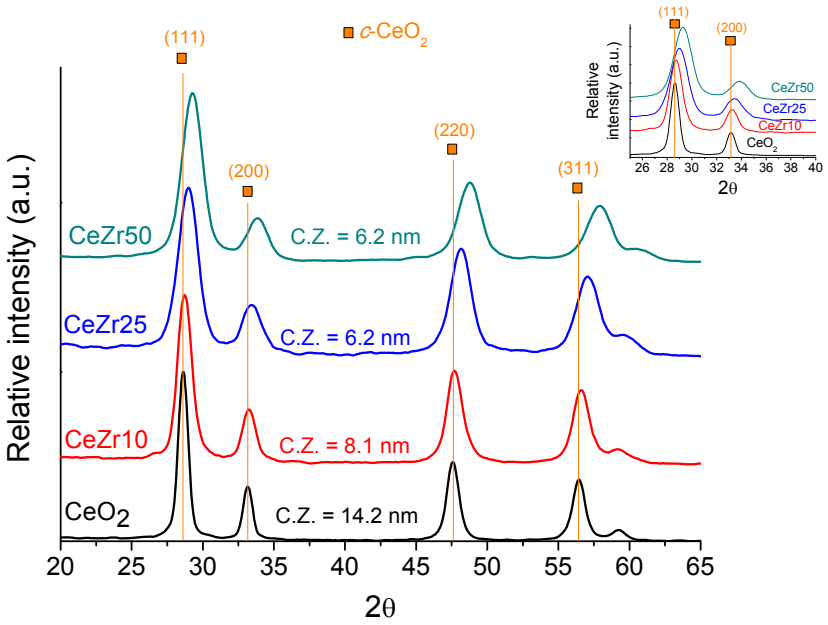
c-CeO2
(111)
(200)
(220)
(311)
CeZr50
CeZr25
CeZr10
CeO2
C.Z. = 6.2 nm
C.Z. = 6.2 nm
C.Z. = 8.1 nm
C.Z. = 14.2 nm
Relative intensity (a.u.)
2θ
20 25 30 35 40 45 50 55 60 65
Relative intensity (a.u.)
26 28 30 32 34 36 38 40
2θ

Figure 2

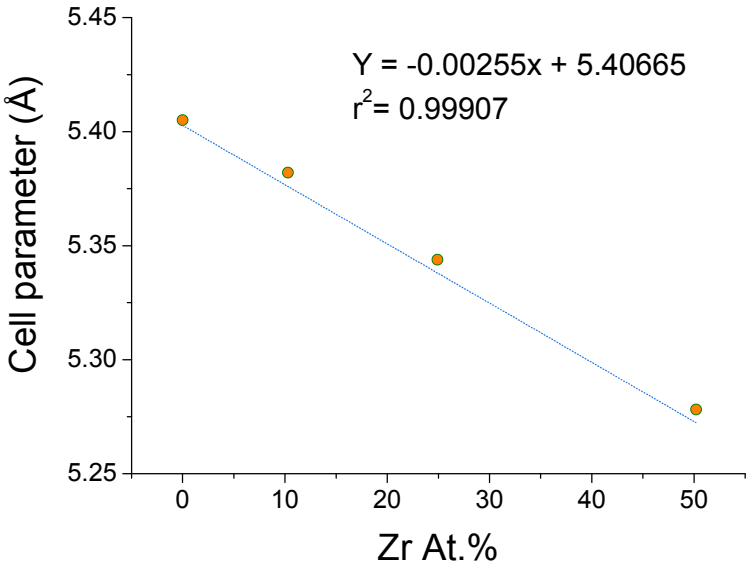
Y = -0.00255x + 5.40665
r2= 0.99907
Cell parameter (Å)
5.45
5.40
5.35
5.30
5.25
0
10
20
30
40
50
Zr At.%

Figure 3

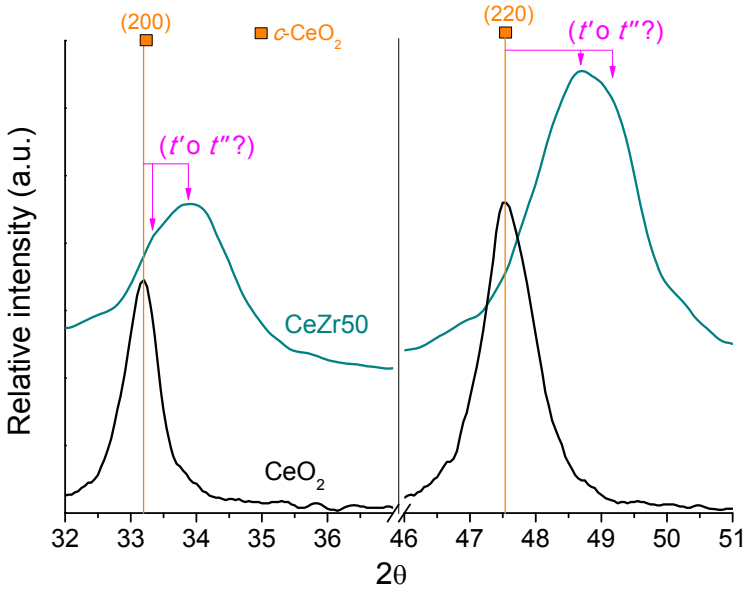
(200)
c-CeO2
(t′o t″?)
(220)
(t′o t″?)
CeZr50
CeO2
Relative intensity (a.u.)
32
33
34
35
36
46
47
48
49
50
51
2θ

Figure 4

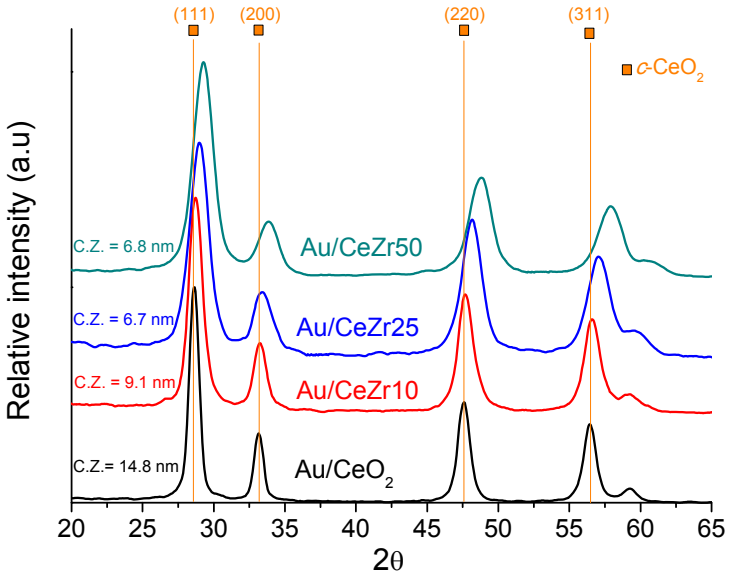
(111)
(200)
(220)
(311)
c-CeO2
Relative intensity (a.u)
C.Z. = 6.8 nm
Au/CeZr50
C.Z. = 6.7 nm
Au/CeZr25
C.Z. = 9.1 nm
Au/CeZr10
C.Z.= 14.8 nm
Au/CeO2
20
25
30
35
40
45
50
55
60
65
2θ

Figure 5

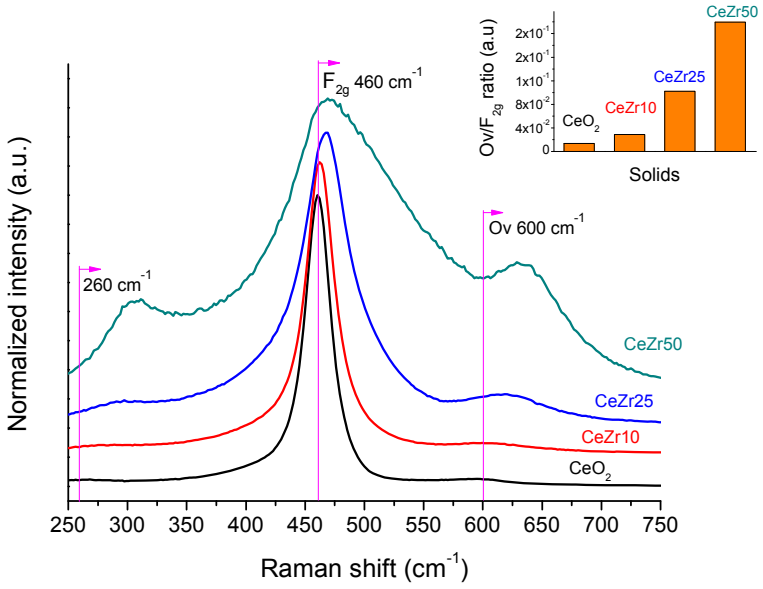
Normalized intensity (a.u.)
Raman shift (cm-1)
F2g 460 cm-1
260 cm-1
Ov 600 cm-1
CeZr50
CeZr25
CeZr10
CeO2
Ov/F2g ratio (a.u)
Solids

Figure 6

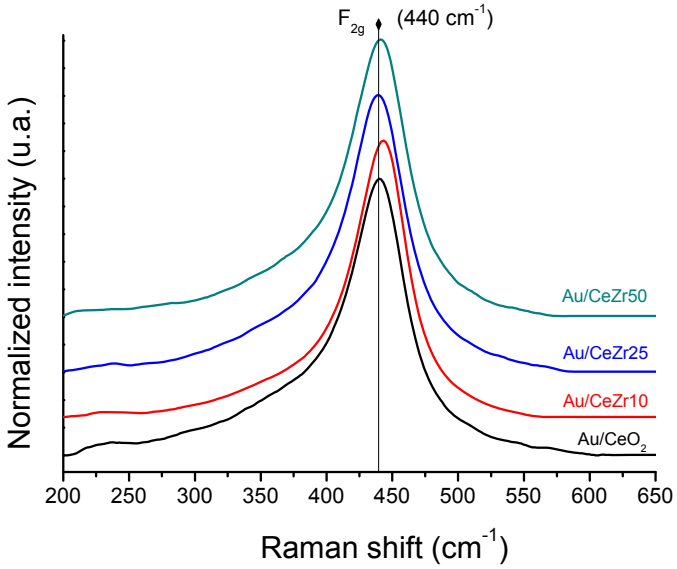
F2g (440 cm-1)
Normalized intensity (u.a.)
Au/CeZr50
Au/CeZr25
Au/CeZr10
Au/CeO2
200
250
300
350
400
450
500
550
600
650
Raman shift (cm-1)

Figure 7

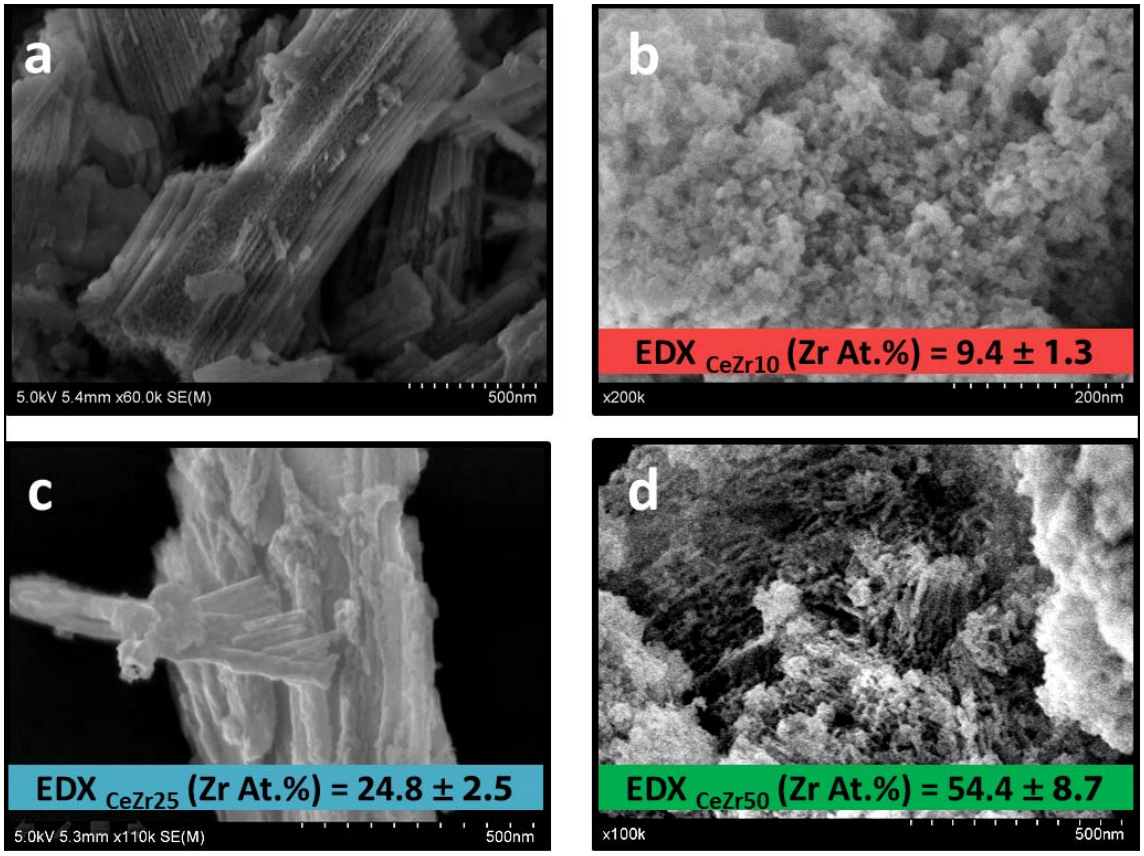
a
5.0kV 5.4mm x60.0k SE(M)
500nm
b
EDX CeZr10 (Zr At.%) = 9.4 ± 1.3
x200k
200nm
c
EDX CeZr25 (Zr At.%) = 24.8 ± 2.5
5.0kV 5.3mm x110k SE(M)
500nm
d
EDX CeZr50 (Zr At.%) = 54.4 ± 8.7
x100k
500nm

Figure 8

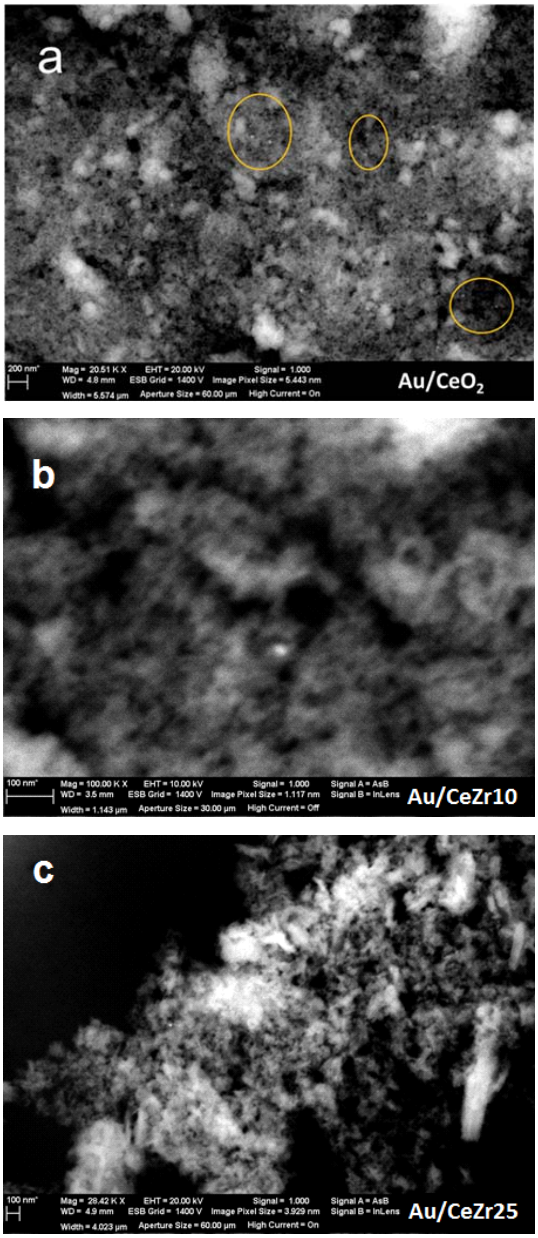
a
200 nm
Mag = 20.51 K X EHT = 20.00 kV Signal = 1.000
WD = 4.8 mm ESB Grid = 1400 V Image Pixel Size = 5.443 nm
Width = 5.574 µm Aperture Size = 60.00 µm High Current = On
Au/CeO2
b
100 nm
Mag = 100.00 K X EHT = 10.00 kV Signal = 1.000 Signal A = AsB
WD = 3.5 mm ESB Grid = 1400 V Image Pixel Size = 1.117 nm Signal B = InLens
Width = 1.143 µm Aperture Size = 30.00 µm High Current = Off
Au/CeZr10
c
100 nm
Mag = 28.42 K X EHT = 20.00 kV Signal = 1.000 Signal A = AsB
WD = 4.9 mm ESB Grid = 1400 V Image Pixel Size = 3.929 nm Signal B = InLens
Width = 4.023 µm Aperture Size = 60.00 µm High Current = On
Au/CeZr25

Figure 9

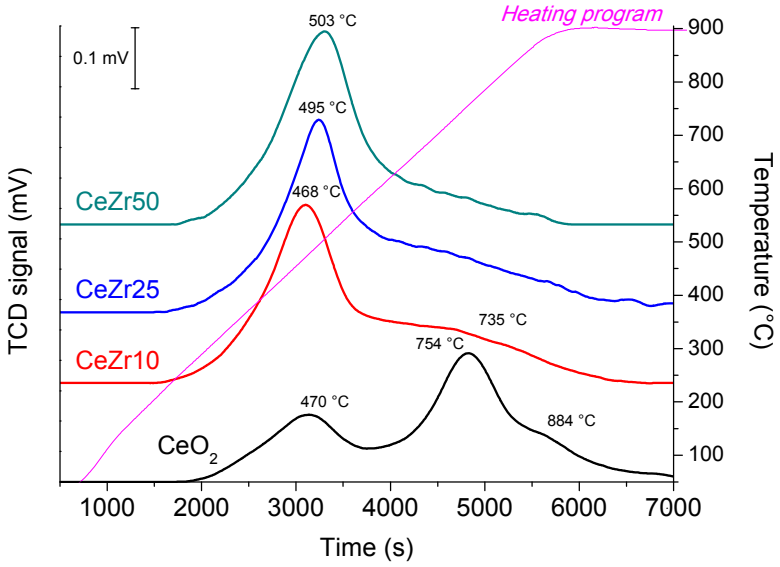
Heating program
503 °C
0.1 mV
495 °C
468 °C
CeZr50
CeZr25
CeZr10
735 °C
754 °C
470 °C
884 °C
CeO2
TCD signal (mV)
Temperature (°C)
Time (s)
900
800
700
600
500
400
300
200
100
1000
2000
3000
4000
5000
6000
7000

Figure 10

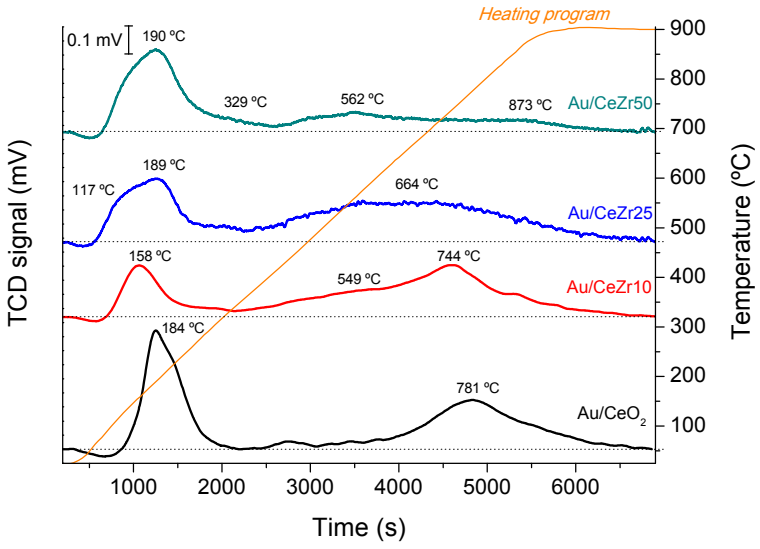
Heating program
0.1 mV
190 ºC
329 ºC
562 ºC
873 ºC
Au/CeZr50
189 ºC
117 ºC
664 ºC
Au/CeZr25
158 ºC
744 ºC
549 ºC
Au/CeZr10
184 ºC
781 ºC
Au/CeO2
TCD signal (mV)
Temperature (ºC)
Time (s)
900
800
700
600
500
400
300
200
100
1000
2000
3000
4000
5000
6000

Figure 11

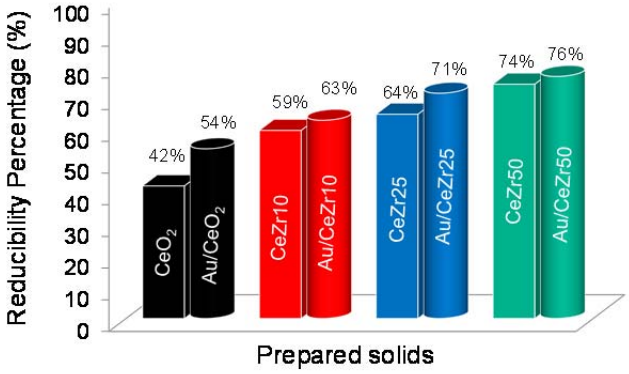
Reducibility Percentage (%)
100
90
80
70
60
50
40
30
20
10
0
42%
54%
59%
63%
64%
71%
74%
76%
CeO2
Au/CeO2
CeZr10
Au/CeZr10
CeZr25
Au/CeZr25
CeZr50
Au/CeZr50
Prepared solids

Figure 12

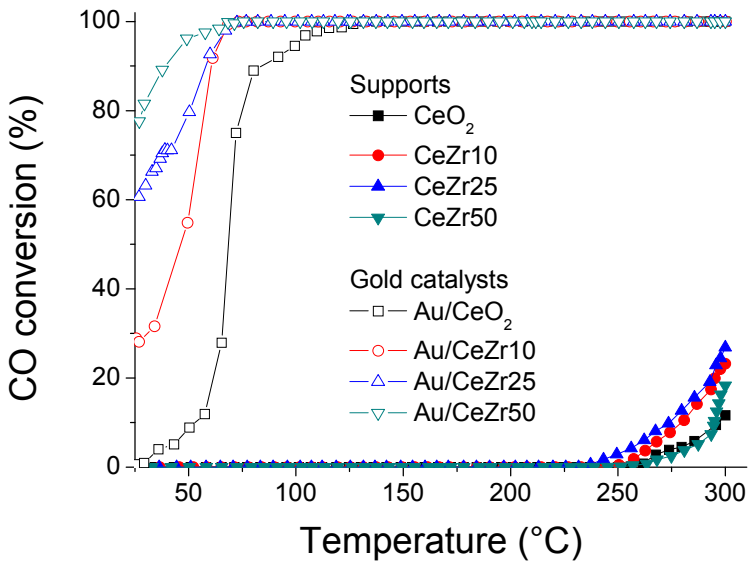
CO conversion (%)
Temperature (°C)
100
80
60
40
20
0
50
100
150
200
250
300
Supports
CeO2
CeZr10
CeZr25
CeZr50
Gold catalysts
Au/CeO2
Au/CeZr10
Au/CeZr25
Au/CeZr50